COUPLED CFD/CSD PREDICTION OF ROTOR AERODYNAMIC AND STRUCTURAL DYNAMIC LOADS FOR THREE CRITICAL FLIGHT CONDITIONS

Jayanarayanan Sitaraman *
Anubhav Datta †
James Baeder ‡
Inderjit Chopra §

Abstract

This paper predicts the UH-60A airloads and structural loads at three critical level flight conditions. A RANS CFD analyses (TURNS) is consistently coupled with a rotor comprehensive analysis (UMARC) to obtain aeroelastic trim solutions from first principles. The focus is on the low speed transition flight, high speed forward flight, and high altitude dynamic stall flight. The CFD analyses uses an overset mesh approach for full wake capture. The comprehensive analysis supplies the rotor CSD model and aircraft trim. The fundamental contribution of CFD is at high speed. The 3D unsteady transonic pitching moments are accurately captured on the outboard blade stations in the advancing side. The accurate elastic twist generated by the CSD model then resolves the advancing blade lift phase, vibratory lift and peak-to-peak pitch link load at this flight condition. At low speed, the vibratory airloads are captured by CFD with the same level of accuracy as state-of-art free wake models. However, the 3/rev flap bending moment, the critical structural load at this flight remains poor. At the high altitude stall flight, the two retreating blade cycles are predicted with reasonable accuracy. Unlike the high speed and low speed cases, predictions are significantly affected by turbulence modeling. The high frequency torsion loads, the key structural loads at this flight, the captured in magnitude but not in phase. The peak-to-peak pitch link loads are well predicted at all flight conditions.

*Assistant Research Scientist, Alfred Gessow Rotorcraft Center
†Assistant Research Scientist, Alfred Gessow Rotorcraft Center
‡Associate Professor, Alfred Gessow Rotorcraft Center, Department of Aerospace Engineering, University of Maryland
§Professor and Director, Alfred Gessow Rotorcraft Center, Department of Aerospace Engineering, University of Maryland

Introduction

The highly unsteady loading caused by the combined effect of blade dynamics, aerodynamic interactions and complex aerodynamic-structural coupling makes the rotorcraft aeroelastic analysis one of the most difficult problems to be modeled. Comprehensive aeroelastic analysis methodologies which used lifting line based aerodynamic models have shown poor prediction trends for rotor loads (Ref. 1). Datta et.al (Ref. 2) performed a series of studies decoupling the structural and aerodynamic models to asses their respective accuracies in load prediction. This study indicated that the structural dynamic model is sufficiently accurate compared to the lifting line based aerodynamic model which suffered from significant inaccuracies. The primary inaccuracy of the lifting line model was found to be the inability to accurately resolve the pitching moments on the advancing side of the blade at high speed flight condition, where transonic effects are prevalent. These observations provided motivation for improving the aerodynamic modeling in the comprehensive aeroelastic analysis.

A way of improving the aerodynamic modeling is to use a coupled CFD/CSD analysis. The coupled CFD/CSD approach replaces the lifting line aerodynamic model in the comprehensive analysis with a higher fidelity Computational Fluid Dynamic model that uses the Reynolds-Averaged Navier-Stokes (RANS) equations. Recently, considerable improvements in airload prediction was demonstrated using the coupled CFD/CSD approach by various research works (Refs. 3–7). Datta and Sitaraman (Ref. 3) examined airloads and structural loads at high speed using CFD/CSD coupling. Datta (Ref. 7) further investigated aerodynamic loads and structural loads at the high altitude stall case. The CFD approach used in these efforts used single blade CFD calculation that was coupled to a freewake approach for the induced inflow. Potsdam et. al (Ref. 4) examined CFD/CSD coupling at

all the three level flight conditions and also hover. The focus of this effort was restricted to the aerodynamic load prediction using full wake capturing from CFD.

It was observed from the aforementioned research efforts that the CFD/CSD coupling improved the prediction of pitching moments, specifically for the high speed forward flight condition. The present paper focuses on both aerodynamic loads and structural dynamic loads at all the three flight conditions and also examines the underlying physical phenomenon.

The primary objective of this paper is to evaluate improvements produced by the coupled CFD/CSD approach for both aerodynamic and structural dynamic loads. The study will focus on three critical helicopter flight conditions. a) high speed forward flight case where transonic effects are important, b) a high thrust case where effects of dynamic stall are evident and c) a low speed forward flight case where effects of wake interactions are present. Efforts will be focused also on assessing the ability of the CFD based aerodynamic model in resolving the fundamental physics that characterize the airloads at these flight conditions. All the predictions are validated with the UH-60A ((Ref. 8)) data.

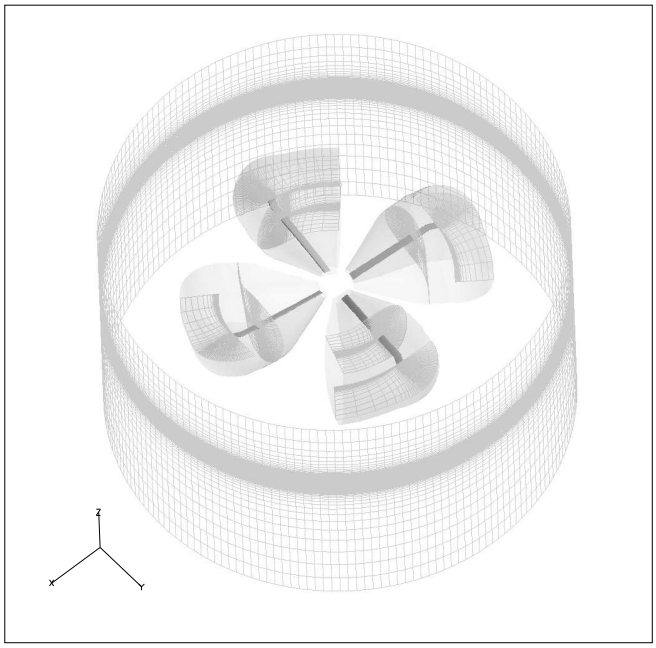

Figure 1: **Overset grids system used for CFD computations**

Methodology

The CFD/CSD approach uses a loose coupling methodology (Ref. 9) for exchange of data between the structural and aerodynamic models. The RANS solver used as the CFD analysis is the University of Maryland Transonic Rotor Unsteady Navier Stokes (UMTURNS). The University of Maryaland Rotor Comprehensive Analysis Code (UMARC) serves as the platform for the aeroelastic analysis by providing the CSD model, rotor trim and the lifting line based aerodynamic modeling.

CFD methodology

The UMTURNS code uses a finite difference numerical algorithm that evaluates the inviscid fluxes using an upwind-biased flux difference scheme. The van Leer monotone upstream-centered scheme for conservation laws (MUSCL) is used to obtain third order spatial accuracy combined with flux limiters to make the scheme Total Variation Diminishing (TVD). The viscous terms are computed using second order central differencing. The viscous fluxes are evaluated in all the three directions including that caused by the cross derivatives.

The Spalart-Allmaras (Ref. 10) turbulence model is used to close the RANS equations. Many experimental (Ref. 11), (Ref. 12) and analytical (Ref. 13) studies on tip vortices have reported largely reduced turbulence levels in the vortical core, which is attributed to the near solid body rotation that appears in the core. To account for this effect, the Spalart-Allmaras turbulence model which was originally developed in a wall-based framework, have to be modified. A simple correction for the production term as suggested by as (Ref. 14) and (Ref. 15) is used.

The present numerical scheme employs a modified finite volume method for calculating the grid and time metrics. The aeroelastic deformations are included in the flow solutions by moving the mesh points to conform to surface geometry of the deformed blade in a consistent manner. A dynamically deforming mesh geometry requires the recomputation of the space and time metrics at every time step. These quantities are calculated such that the Geometric Conservation Law (GCL) is satisfied at all times.

A second order backwards difference along with Newton-type sub-iterations is used for marching in time. The Newton sub-iterations eliminate the factorization and linearization errors and restore the formal second order accuracy.

Grids and Boundary conditions

An overset mesh based approach is used. This approach utilizes body conforming meshes for the rotor blades (near body grids) that are encapsulated in a cylindrical back-

ground mesh. The background mesh is appropriately clustered to provide sufficient resolution for capturing regions of concentrated vorticity. The grids used are illustrated in Figure 1

All the near body grids were generated using a C-O hyperbolic grid, which generates C-type grids for two dimensional sections. The three dimensional grids were constructed by stacking and bending the two dimensional grids. At the tip region, the mesh planes are rotated about the chord-line and appropriately redistributed to form a smooth definition of the tip. Therefore, the resulting grid is C-type in the wraparound direction and O-type in the span-wise direction. The background mesh is constructed in polar coordinates with algebraic redistribution to improve the resolution in the wake regions.

Boundary conditions are specified explicitly. The viscous wall boundary condition is incorporated at the rotor blade surface. The pressure along the body surface is calculated by solving the normal momentum equation. The equation of state is used to obtain the total energy from the other conserved variables. Continuity across the wake cut is maintained by averaging the flow variables on both sides of the planes. The outer lower boundaries of the background mesh are updated using a characteristic type boundary condition. The flow variables at the boundary are determined such that they satisfy the Riemann invariants from the theory of characteristics. The boundary condition adjusts itself depending on the direction of flow (into or out of the boundary).

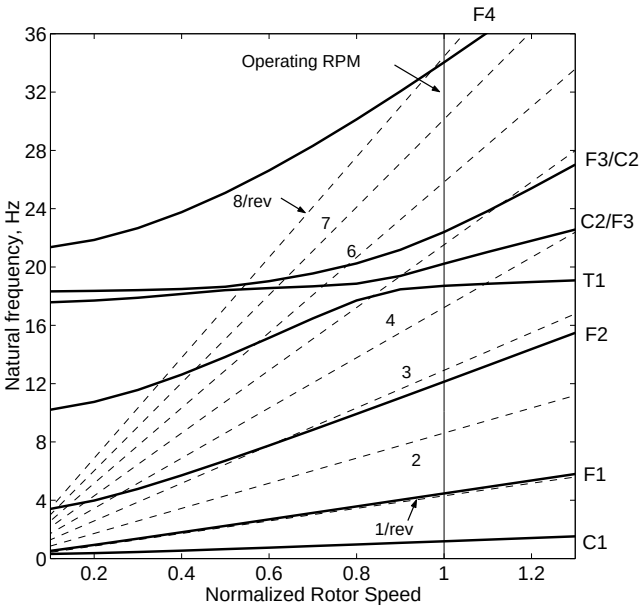

Figure 2: **UH-60A rotor blade frequencies; Collective Angle 14.5 degrees; Effective root spring stiffness 1090 ft-lbs/degree; F:Flap, C:Chord-wise, T:Torsion; Operating frequencies: 0.28, 1.04, 2.82, 4.3, 4.7, 5.2, 7.9, 11.3, 12.4 and 12.6/rev**

Hole cutting and Chimera interpolation

All computations are performed in the inertial frame. The near-body meshes move with respect to the background mesh as a consequence. Therefore at every time step a hole cutting is performed on the background mesh that accounts for the current location of the near body meshes. The donor cells and receiver points for mutual interpolation between the near-body and background meshes are also determined. An algorithm that uses an octree based search for localization and stencil jumping for exact cell determination is used to aid both the holecutting and connectivity calculation. A minimal bounding box estimated using inertial bisection is used for accelerating the hole cutting process. There is an overlap region extending 2 chord distances between the near-body and background meshes.

CSD model

The rotor blades are modeled as second-order nonlinear, isotropic Euler-Bernoulli beams. The coupled flap-lag-torsion equations are based on (Ref. 16). The formulation is extended to include axial elongation and elastic twist as quasi-coordinates, based on References (Ref. 17) and (Ref. 18). The resultant almost-exact beam model is accurate up to moderate bending deflections of 15% (Ref. 19). The rotor blade is treated as a fully articulated beam with flap and lag hinges coincident at 4.66% span. All blades are identical. Each blade is discretized into 20 finite elements undergoing flap, lag, torsion and axial degrees of motion. The blade property data, including nonlinear structural pre-twist and sweep are obtained from the NASA (Ames) master database. The nonlinear lag damper force is imposed on the structure as a set of concentrated forces and moments acting at 7.6% of the blade span. The pitch link is modeled as a linear spring-damper system. The elastomeric bearing stiffness and damping are modeled as linear springs and dampers in flap, lag and torsion. The first eight structural modes are used for the present study. The rotor blade frequency plot and the first ten natural frequencies at the operating RPM are shown in Figure 2. These correspond to a collective angle of 14.5 degrees and a measured root torsion spring stiffness of 1090 ft-lb/degree (Ref. (Ref. 20)). The root spring stiffness is an equivalent measure of the pitch link stiffness.

Validation of UMARC CSD model

Measured airloads, damper force and control angles are used to calculate and validate the structural response of an isolated rotor. Prediction errors originate mainly from structural modeling, and errors in airload measurements.

The measured airloads problem is ill-posed because the airloads are fixed and do not change in response to blade deformations. This leads to zero aerodynamic damping. It cannot be solved for all rotor systems. Consider a teetering, gimbaled or articulated rotor with fundamental flap frequency of 1/rev with zero structural damping. If the measured aerodynamic hinge moment is accurate, the 1/rev component will be identically zero in which case the rotor response is undefined. This is because, at resonance, the damping force is equal and opposite to the forcing and they are both included within the measured airloads. In practice, errors in measurements will produce a non-zero 1/rev aerodynamic hinge moment which will drive the rotor response to infinity. For non-zero structural damping, the response will not be infinite but the accuracy of the measured airloads required for a reasonably accurate response solution will be extremely high. The point is: the measured airloads problem is highly sensitive to small errors in airloads as well as small changes in rotor parameters. For example, increasing the first torsion frequency from below 4/rev to above 4/rev (due to uncertainty in pitch link stiffness) changes the phase of 4/rev torsion response by 180 degrees. This is not the case for a coupled solution with damping, where the pitch link stiffness has no significant effect on the torsion loads (Refs. 20, 3). The UH-60A blade frequencies are reasonably well separated from the excitation harmonics (Fig 2). The UH-60A rotor properties, both structural and aerodynamic, are well documented. The airload measurements are highly repeatable and accurate.

The airload measurements are on the deformed blade. They are reduced to the undeformed frame iteratively using calculated deformations and the flight test control angles at each step. The periodic blade response is calculated directly using finite element in time. A time-marching algorithm, in comparison, requires more than an order of magnitude longer in computation time to settle down to the final steady-state response. This is because, in the absence of aerodynamic damping, artificial damping is required in the beginning to decay the natural mode response. Subsequently, this damping must be entirely removed to obtain the final steady state solution free of artificial damping.

Figure 3 shows the predicted structural loads for the three flight conditions. The steady components have been removed for comparison. The flap bending moment is pre-dominantly 3/rev at low speed. At high speed, the 1, 2 and 3/rev harmonics are equally dominant and determine the peak-to-peak loading. The 3/rev component is the dominant vibratory harmonic. The high altitude stall case shows the same trend as the high speed case. The peak-to-peak loading is lower because of reduced 1 and 2/rev loads. The analysis captures the trends correctly.

The torsion moment is relatively benign at low speed. The highest peak-to-peak variation occurs at high speed because of large 1 and 2/rev harmonics. These are caused by large transonic pitching moments occurring at the outboard stations. The high altitude flight generates high frequency stall loads at 3-7/rev. The pitch link loads follow a similar pattern. They are benign at the low speed, has mainly lower frequency content at the high speed, and show significant presence of higher frequencies at the high altitude flight. At the low speed, the major contributors are 1 and 4/rev. While at the high speed, a large 1/rev peak oscillation is present on the advancing side. This stems from the large transonic pitching moment variation on the advancing side. In addition, there is significant 2-4/rev content in loads. At the high altitude flight, the peak load is again dominated by a large 1/rev. However, there are significant higher harmonics, 2-6/rev that are generated by dynamic stall. In general, the structural model captures the low frequency components accurately. Discrepancies are present in the predictions of higher harmonics, i.e. 4/rev and above.

The root chord bending moments, at 11.3% R, are dominated by the damper loads at all three flight conditions. The waveforms are well predicted in all cases.

In summary, the key structural load at low speed is the 3/rev flap bending moment. The key loads at high speed are the 3-5/rev flap bending moment and peak-to-peak pitch link load. The key loads at stall are the high frequency torsion 3-5/rev. The high frequency torsion determines the high frequency pitch-link load which subsequently determines the 4/rev servo load in the fixed frame.

CFD/CSD coupling methodology and trim procedure

The CFD and CSD methodologies are tied together in a "loosely coupled" system, i.e. the data is exchanged every revolution of the rotor or in other words after obtaining a periodic solution.

The CFD airloads (normal force, pitching moment and chord force) are coupled at all radial stations from the root cut out to the tip. The airloads and blade deformations are transferred between CFD and comprehensive analysis at all spanwise grid points available in the respective codes. The comprehensive analysis accepts CFD airloads at 120 gauss points and provides blade deformations at the same points. The blade deformations are interpolated radially using cubic splines to the CFD mesh locations. The azimuthal discretization in CFD is an order of magnitude

smaller than that used in CSD. Therefore the blade deformations are also spectrally interpolated in the azimuthal direction for the CFD calculations.

The comprehensive analysis provides the CSD model, a lifting-line model, and the aircraft trim model. The CSD model is same as that described above, except that the measured lag damper force is not used. The lifting-line model provides the air load sensitivities to blade deflection.

The trim model is a free flight propulsive trim for the entire aircraft. The three rotor control angles (collective, longitudinal and lateral cyclic angles), aircraft longitudinal and lateral tilts, and the tail rotor collective are calculated based on force and moment balance about the aircraft center of gravity. The fuselage aerodynamic properties are incorporated as functions of fuselage tilt. Fuselage dynamics is neglected. The aerodynamic properties are obtained from $1/4$-scale wind tunnel experimental data (from Ames database). They include the effect of the horizontal tail. The zero-angle fuselage flat plate area is 36.34 ft^2 (Ref. 26). The tail rotor properties and vertical tail cant angle are included. The main rotor has a three degree forward shaft tilt angle. The details of the propulsive trim analysis and validation are described in (Ref. 2). The lifting line model is described in the next section.

The coupling is performed using the following iterative steps.

1. A lifting-line comprehensive analysis solution is obtained. This provides the baseline blade deformations, trim angles, air loads.

2. Using the baseline solution, CFD air loads are calculated. These air loads are different from, and in general improved, compared to the baseline air loads.

3. The difference between the CFD air loads obtained in step 2 and lifting-line air loads are the *delta* air loads. The lifting-line analysis is now re-run with the delta air loads imposed in addition to the intrinsic lifting-line air loads. The delta air loads are held fixed over the trim iterations. The lifting-line air loads change from one trim iteration to another and provide the air load sensitivities required to trim the rotor. In addition, the lifting-line air loads provide aerodynamic damping which makes the loose coupling procedure well-posed and stable.

4. Step 2 and Step 3 is one CFD/CSD coupling iteration. The coupling iterations are performed until the delta air loads converge at every radial and azimuthal station.

The converged air loads are CFD air loads. They are equal to the converged lifting-line air loads plus the converged delta air loads. The converged delta airloads depend on the lifting-line analysis used, but the converged airloads are independent of the lifting-line solution.

Lifting line based aerodynamic modeling

The UMARC lifting-line model combines a Weissinger-L type near wake (Ref. 22), Bagai-Leishman pseudo-implicit free wake (Ref. 23), airfoil property data (Ref. 24), and Leishman-Beddoes 2D unsteady model for attached, separated and dynamic stall flows (Ref. 25). The model parameters are extracted for the two UH-60A airfoils, using SC1095 and SC1094 R8 static data. The W-L model is combined consistently with the airfoil property tables and stall model. In the first step, the geometric angle of attack is obtained using the blade deformations and far wake inflow. A uniform far wake inflow is assumed in the first step. The angle of attack thus obtained is used to calculate the spanwise bound circulation distribution using airfoil properties. In the second step, a near wake trailer sheet is layed out over thirty degree azimuth following the blade. Twenty five blade segments are used. The bound circulation line is at local quarter-chord and swept back at the tip. The trailer sheet follows the local incident velocity. It is allowed to trail in the reverse direction, in the regions of reverse flow. The velocity induced at the local three-quarter chord is then used to reduce the geometric angle of attack to an effective angle of attack. In the third step, the effective angle of attack distribution is used to modify the bound circulation distribution. Step three and one are repeated until the bound circulation converges. A relaxation scheme is necessary for modifying the bound circulation strengths (10% used here). Finally the bound circulation strengths are consistent with the near wake trailers and airfoil properties. The three steps above form one near wake iteration. Based on the bound circulation strengths, the far wake is recalculated. The Leishman-Beddoes model is then applied at each section on the effective angle of attack distributions.

The baseline free wake uses a single tip vortex model. The vortex is assumed to be fully rolled up, with a strength equal to the maximum bound circulation occurring outboard of 50% span. It is trailed from the tip of the swept elastic axis. This model is used for the low speed and high altitude flight conditions. For the high speed case, a dual vortex model is used. In the dual vortex model, a negative vortex is trailed from the tip in the regions of negative lift. The strength of the negative vortex equals the maximum negative circulation attained near the tip. The positive vortex continues trailing from an inboard radial station. This station is taken at the zero bound circulation cross-over point. The strength of the positive vortex is equal to the sum of the maximum bound circulation occurring outboard of 50% blade radius and the maximum

negative circulation occurring near the blade tip. The latter is non-zero only in the azimuths of negative lift. All vortices are free. The azimuthal and wake age discretization are 5 degrees each respectively. Two turns of the wake are considered. Increasing the discretization angle, or the number of turns did not change the airload predictions.

Computation specifics

Two sets of grids of different resolution are used for the CFD calculations. The medium resolution grids used 0.8 million points each for the near body meshes and 2.2 million points for the background mesh. The fine resolution mesh used 1.2 million points each for the near body meshes and 12 million points for the background mesh. The time integration was performed at a 0.25 degree azimuthal step for all calculations. All computations were performed in a parallel environment on a x86-64 cluster with a processor speed of 3.2 GHz. The time taken per time step/per grid point is found to about 7.8μ seconds. It is worth noting that a converged aeroelastic solution that satisfies the rotor trim equations can be achieved within 10 CFD/CSD coupling cycles, which takes a wall clock time of about 160 hours for the medium resolution meshes on 4 CPU's.

Results

The results presented in this paper are organized as follows. Results are presented first for the high speed, then the stall condition and finally the low speed. First, all the sectional aerodynamic load time histories that were calculated using the CFD/CSD coupling would be presented. They are compared with the flight test data and the corresponding predictions from just the lifting line based comprehensive rotor analysis (UMARC). This is to demonstrate the improvements or short comings the CFD/CSD coupling brings to the prediction of aerodynamic loading. Next, a set of results that encompass flow visualizations and contour plots would be presented to bring out the physics that is critical to these flight conditions. Finally the structural dynamic loads are presented, comparing predictions with the flight test data and corresponding predictions from the lifting line comprehensive analysis code. An assessment of the improvements that CFD/CSD coupling brings to the load prediction is summarized at the end.

The CFD/CSD coupled prediction would be annotated as CFD and the comprehensive analysis predictions would be annotated as Lifting-line in all plots.

High Speed forward flight case (Counter 8534)

This flight condition is at an advance ratio μ of 0.368 and a blade loading (C_w/σ) of 0.0783. The hover tip Mach number M is 0.6415 and the lock number for this flight condition based on ambient density is 6.33.

Sectional aerodynamic loads

The time history of sectional normal forces at 9 radial stations (where flight test data is available) is depicted in Figure 4. It can be observed that the CFD/CSD coupling shows improvement in phase in all the radial stations. The advancing side waveform is well predicted 60% outboard. The lifting line analysis on the other hand shows a large phase error on the advancing side. The peak to peak magnitudes of normal forces are not as inaccurate as the phase prediction. Also, it is to be noted that the sectional waveforms show relatively large discrepancies in the radial stations located between 60% and 80% span.

Figure 5 shows the sectional airloads after a low frequency filter has been applied. Here the steady and first two harmonics are removed. The remaining (3/rev and higher) harmonics are the dominant contributors to fixed frame vibration in the case of UH-60A as it has a 4 bladed rotor system. It is clear from the plot that the phase error in the sectional airloads (in the case of lifting line aerodynamic model) originates from the inaccurate prediction of the vibratory aerodynamic loads. The CFD/CSD prediction, however shows much improved prediction of the vibratory airloads. The reasons that are attributed to the improved prediction are discussed in detail in the following section.

The sectional pitching moment time histories are shown in Figure 6. The CFD/CSD prediction shows much better correlation in both phase and magnitude compared to the prediction from the lifting line aerodynamics, especially on the advancing side. It should be noted that the advancing rotor flow field is characterized by a transonic flow field. The lifting line aerodynamic model is inadequate in resolving the pitching moments in this transonic region.

The correlation with data at the 77.5% station appears unsatisfactory at this flight condition. The source of this discrepancy is attributed to the trim tab that is located at this radial station. The angle of the trim tab on the test aircraft is unknown and hence not modeled.

Modeling of the fundamental physics

There are two key physical phenomena that dominate the nature of the sectional aerodynamic load time histories at this flight condition. They are a) Three dimensional unsteady transonic effects on the advancing side and b) Wake interactions at the inboard radial stations caused by

the vorticity shed from negatively loaded tip of preceding blade. The effects of these key phenomenon are illustrated in Figure 7. It is worth noting that the wake interaction is a secondary effect and is triggered only in the presence of the first.

The transonic flow field creates moving shock waves on the advancing side, that causes the aerodynamic center to travel towards the trailing edge giving rise to large nose-down pitching moments. The moving shocks are relieved towards the tip region because of the three dimensional nature of the flow field. Therefore, the movement of aerodynamic center would be lesser than that would be predicted by just accounting for two dimensional compressibility effects. This is one of the major deficiencies of the lifting line aerodynamic modeling as it accounts only for the 2-D compressibility effects through a Mach number based table lookup. In the CFD model the three dimensional unsteady transonic effects are accounted more accurately. The nose-down pitching moments produces large 1/rev elastic twist. The 1/rev elastic twist is phased in such a manner that it causes the rotor blade to elastically twist nose-down on the advancing side producing negative lift at the tip regions. The CFD-CSD approach gives good predictions for the sectional pitching moments and hence an improved prediction of elastic twist deformations. The improved prediction of elastic twist resolves the prediction of the phase and magnitude of the advancing blade lift.

The vortex sheet shed from the rotor blades in general rolls up in to a concentrated tip vortex within 30 to 40 degrees of wake age. However, the presence of negative lift on the rotor causes significant changes in the roll up phenomenon. From Fig 7(a) it can be observed that there is strong inboard vorticity which rolls upwards and weak tip vortex with a negative (clockwise rotation) vorticity that is rolled up downwards. The strong inboard vortex sheet is pushed upwards because of the mutual interaction with the negative tip vortex. The inboard sheet also starts to roll up in to a concentrated vortex. This strong inboard vorticity interacts with the following rotor blade. The effects of this interaction is most prominent in radial stations between 60% and 80%. The impulsive loads thus created dominates the vibratory airload time history in the radial stations at these mid-span locations. The prediction of these interactions also improves the phase of the negative lift at the radial locations closer to the tip.

Structural dynamic loads

Figure 8 shows predicted structural loads at high speed. The flap bending moments from CFD/CSD coupling show improved prediction on the advancing side. The waveform on the advancing side is affected strongly by the advancing side lift waveform at the inboard stations (67.5% R and 77.5% R) (Ref. 3). Accurate lift at the inboard stations require accurate elastic twist and accurate inboard wake interactions. The inboard wake interactions are caused by positive vorticity moving inboard in the regions of negative lift. Accurate twist is generated by the CSD model in presence of accurate transonic pitching moments captured by CFD. Prediction of transonic pitching moment is the most significant contribution of CFD. This is a fundamental improvement which provides the correct twist, which, along with a refined wake model resolves the long standing problems of high speed vibratory lift and advancing side lift phase. The fundamental improvement is reflected in the torsion loads. The peak-to-peak pitch-link load, advancing blade waveform, and the lower harmonics are well captured. The discrepancy on the retreating side stems from higher harmonic errors, and are not fully resolved even with measured airloads and damper loads as shown earlier (figure 3). The vibratory flap bending moments are shown in figure 9. The 3 and 4/rev, even though not accurate, show the correct trends as obtained by measured airloads. The key discrepancy here is in the prediction of 5/rev. The 3 and 4/rev harmonics are affected mainly by elastic twist. The 5/rev harmonic is contributed mainly by the wake.

High Altitude Stall case (Counter 9017)

This flight condition is at an advance ratio μ of 0.237 and a blade loading (C_w/σ) of 0.133. The lock number for this flight condition based on ambient density is 4.02.

Sectional aerodynamic loads

Figure 10 shows the time history of sectional normal forces at the various radial stations. The steady value of the flight test appears to have some uncertainty in this flight condition. Therefore the steady value is removed for plotting purposes. The sectional airloads show a minimum in the first quadrant because of the low angle of attack on the advancing side that is caused by the elastic twist. Unlike the high speed case the lift does not go negative in this region. The other major characteristic of the sectional normal force time history is the undershoot produced by dynamic stall effects in the fourth quadrant. The pitching moment time history shown in Figure 11 show more interesting features in the stall region. There are two undershoots in the fourth quadrant indicating that the blade stall twice in the radial stations between 60% and 95%.

The CFD/CSD predictions do capture all the essential features in sectional airload time histories. However, there is still considerable phase differences in the location of the stall peaks, especially evident in the pitching moments.

Modeling of fundamental physics

The key physical phenomenon that dominates this flight condition is the dynamic stall that happens on the retreating side. Figure 12 illustrates the stall phenomenon. The first stall in the pitching moment is caused just by the effective angle of attack caused by the large blade pitch. A large 4,5/rev excitation in torsion is caused by this stall impulse in the pitching moment. This torsional excitations causes the blade to stall again within 30 degrees of the first stall. Most of the outboard portion of the blade shows the stall phenomenon. The greatest extent of stall is observed at the 90%location. The CFD/CSD approach is fairly accurate in capturing the stall and the related aeroelastic effects.

Structural dynamic loads

Figure 13 shows predicted structural loads at the high altitude flight. Compared to the two high vibration regimes this flight condition is benign in vibration. The focus here is to capture the high frequency stall loads (3/rev and higher) in torsion. They determine the pitch-link load, and servo loads in the fixed frame. The limiting design loads encountered in the severe maneuvers are very similar to the stall loads encountered here. The high frequency torsion loads show significant improvements from the CFD/CSD coupling. However, the peak-to-peak loads are captured equally well by a lifting-line model. The torsion harmonics are compared in figure 14. Compared to predictions using measured airloads, significant errors occur in 4 and 5/rev. The 5/rev error is not resolved even with measured airloads, and stems from discrepancy in the structural model.

Low speed flight case (Counter 8515)

This flight condition is at an advance ratio (μ) of 0.110 and a blade loading (C_w/σ) of 0.0782. The lock number for this flight condition based on ambient density is 6.59.

Sectional aerodynamic loads

The sectional aerodynamic loads for this flight condition is shown in Figure 15. The time history shows peaks, one on the advancing side and one on the retreating side. These peaks are caused by the inflow variation induced by the rolled up intertwined wake structure on either side of the rotor disk. The CFD/CSD predictions capture the basic physics correctly. The vibratory sectional normal forces are shown in Figure 16. Again, the impulsive loads caused by the wake interaction dominates the vibratory airloads The correlation with the flight test data is less satisfactory at the inboard radial stations. There is considerable amount of higher harmonic content in the flight test data which are not resolved accurately by the CFD/CSD approach. Figure 17 shows the sectional pitching moment time history. As in the case of the normal forces, the pitching moment correlation also becomes worse at the inboard radial stations.

Modeling of fundamental physics

The intertwined wake structure is the key physical phenomenon that dictates the airload time history at this flight condition. The rotor tip vortices intertwine and coalesce in bigger vortex structures as if they were shed from a circular flat plate. This wake structure causes impulsive variation in the induced inflow over the rotor disk at advancing (60-90 degree) and retreating (270-310 degrees) on the rotor disk. The effective angle of attack and hence the sectional aerodynamic loads also exhibit the same variation as the induced inflow distribution. The rolled up wake structure predicted from CFD calculations and their influence on the blade aerodynamic loads is illustrated in Figure 18.

Structural dynamic loads

Figure 19 shows predicted structural loads at low speed. The flap bending moments are unsatisfactory. The predominant 3/rev vibratory harmonic is missed by both analyses. The peak-to-peak torsion loads are satisfactorily predicted by both. The vibratory flap bending moments are studied in figure 20. The magnitude and phase of 3, 4, and 5/rev harmonics are plotted over blade span. CFD/CSD predictions are compared with predictions using measured airloads (corresponding to figure 3 earlier). Predictions are similar for 4, and 5/rev. The key discrepancy clearly is in the prediction of 3/rev. The problem is currently under investigation.

Assessment of CFD/CSD prediction capability

Airload predictions are significantly improved by CFD/CSD coupling. The improvements are not enough to accurately capture the structural loads. Key deficiencies remain in the prediction of 3/rev and higher loads. A summary is provided below for the three flight conditions.

At the high speed, the airload predictions show a fundamental improvement. The 3D unsteady transonic pitching moments are captured accurately at the outboards stations on the advancing side. Predictions show fair grid and time step convergence at this flight condition. The inboard wake effects appears to be resolved, eventhough there is a large margin for improvement with better grid resolution. The peak-to-peak torsion moment and pitch

link load are accurately predicted. However prediction of 3/rev and higher harmonics that are important for 4/rev servo loads in the fixed frame, are unsatisfactory. This deficiency is not resolved even when using the measured airloads. The flap bending moments show a phase discrepancy of around 7-10 degrees compared to CSD predictions with measured airloads.

At low speed transition, the wake inter-twinning effect appear to be predicted as accurately as state-of-art free wake models ((Ref. 26)). The inter-twinning effect produces the key vibratory airloads, 3-5/rev. In general, the vibratory airloads, 3-10/rev, remains unaffected with increase in grid resolution. The level of grid refinement necessary to capture the higher harmonic caused by wake interactions are not computationally viable at the present time. The numerical diffusion that arises from the discretization of the convective fluxes causes the vortical structures to diffuse much faster than their physical diffusion rate. The current methodology follows a passive grid clustering approach which is insufficient for capturing the wake dynamics accurately. However, it does capture the basic physical phenomenon and the gross effects of the intertwined wake structure on the inflow distribution on the rotor disk. Within the practical limitation of mesh sizes, grid refinement does not appear to alter the 3-10/rev loads, which are the key harmonics behind rotor vibration at this critical high vibration flight. Out of these harmonics, 3/rev is the dominant contributor. Therefore, the prediction of the 3/rev flap bending moment, which is the key structural load at this flight condition, remains poor. Thus the improved airload prediction from CFD/CSD is still not sufficient to predict the vibratory flap bending moment at this flight condition.

Unlike the high speed and low speed transition cases, predictions in the high altitude stall case show a significant dependency on the turbulence model and grid resolution. With a fine grid, the Spalart-Allmaras model, and wake capturing the two retreating blade stall cycles appear to be captured. Dynamic stall is particularly challenging for the CFD approach. Nonetheless, the magnitude of the lift and pitching moment excursions caused by stall are resolved quite satisfactorily. However, the prediction of the onset of the stall and reattachment are unsatisfactory. The key structural loads at this flight condition are the peak-to-peak pitch link load and 3-5/rev torsion moments. The peak loading is captured even by a lifting-line model. CFD/CSD coupling improves the prediction of 3-5/rev harmonics. The improvement is limited to the magnitude. The prediction phase is not yet accurate.

Summary and Conclusions

1. A second order accurate non-linear beam theory satisfactorily predicts the structural dynamic loads on an UH-60A rotor in all three critical flight regimes. The flap bending moments are accurately predicted. The lower harmonics of torsion (1-3/rev) are accurately predicted. Significant discrepancies occur at the higher harmonics.

2. The key improvement provided by CFD is in the prediction of transonic unsteady pitching moments at high-speed forward flight. They occur 80% R outboard of the blade span. Accurate prediction of transonic pitching moments resolves the problem of advancing blade lift phase, vibratory lift and peak-to peak pitch link load at this flight condition.

3. The wake interaction on the advancing side causes the lift impulse on the sectional aerodynamic loads in the first quadrant. This effect is resolved by the CFD model.

4. The phase of the flap bending moment at high speed is not yet accurately resolved. There is an approximate 7-10 degrees phase shift between CFD/CSD predictions and predictions using measured airloads. The higher harmonic pitch link loads remain unresolved. This is a structural dynamic problem because, imposing flight test airloads on the CSD retains similar inaccuracy as the CFD/CSD solution.

5. In the low speed flight, direct capture of the far wake appears correctly predicts the vortex induced loads in the first and fourth quadrants. However, the accuracy is not enough to capture the dominant 3/rev flap bending moments at this flight condition.

6. In high altitude flight, accurate prediction of dynamic stall loads appears to be a significant challenge. Refined CFD grid, turbulence modeling, and consistent wake capture all appear important. The critical loads at this flight condition are the torsion loads. The peak-to-peak pitch link loads, and the 4/rev servo loads in the fixed frame are determined primarily by the torsion loads. Present predictions accurately capture the peak-to-peak pitch link loads. The higher harmonics show errors in magnitude and phase. The errors appear to stem from both aerodynamic as well as structural dynamic modeling.

References

[1]William G. Bousman, “Putting the Aero Back Into Aeroelasticity,” 8th Annual ARO Workshop on Aeroelas-

ticity of Rotorcraft Systems, University Park, PA, October, 1999.

[2]Datta, A., Chopra, I., "Validation and Understanding of UH-60A Vibratory Loads in Steady Level Flight," *Journal of the American Helicopter Society*, Vol. 49, No. 3, July 2004, pp 271-287.

[3]Datta, A., Sitaraman, J., Chopra., I, and Baeder, J., "Analysis Refinements for Prediction of Rotor Vibratory Loads in High-Speed Forward Flight," American Helicopter Society 60th Annual Forum, Baltimore, MD, June 2004.

[4]Potsdam, M., Yeo, Hyeonsoo, Johnson, Wayne, "Rotor Airloads Prediction Using Loose Aerodynamic/Structural Coupling," Presented at the American Helicopter Society 60th Annual Forum, Baltimore, MD, June 7-10, 2004.

[5]Altmikus, A. R. M., Wagner, S., Beaumier, P., and Servera, G., "A Comparison : Weak versus Strong Modular Coupling for Trimmed Aeroelastic Rotor Simulation," American Helicopter Society 58th Annual Forum, Montreal, Quebec, June 2002.

[6]Pomin, H. and Wagner, S. "Aeroelastic Analysis of Helicopter Rotor Blades on Deformable Chimera Grids," *Journal of Aircraft*, Vol. 41, No. 3, May-June 2004.

[7]Datta, A., and Chopra, I., "Prediction of UH-60A Dynamic Stall Loads in High Altitude Level Flight using CFD/CSD Coupling," 61st Annual Forum of the American Helicopter Society, Grapevine, Texas, June 1-3, 2005.

[8]Bousman, G. and Kufeld, R.M., Balough, D., Cross, J.L., Studebaker, K.F. and Jennison, C.D., "Flight Testing the UH-60A Airloads Aircraft", 50th Annual Forum of the American Helicopter Society, Washington, D.C., May, 1994.

[9]Tung, C., Caradonna, F., X. and Johnson, W., "The Prediction of Transonic Flows on an Advancing Rotor," *Journal of American Helicopter Society*, Vol. 32, No. 7, 1986, pp. 4-9.

[10]Spalart, P.R., and Allmaras, S.R., "A One-equation Turbulence Model for Aerodynamic Flows," AIAA Paper 92-0439, 1992.

[11]Devenport, W.J., Rife, M.C., Liapis, S.I., and Follin, G.J., "The Structure and Development of a Wing-tip Vortex," *Journal of Fluid Mechanics, 312*, 1996.

[12]Chow, J.S., Zilliac, G.G., and Bradshaw, P., "Mean and Turbulence Measurements in the Near Field of a Wingtip Vortex," *AIAA Journal, 35(10)*, 1997.

[13]Jacquin, L., and Pantano, C., "On the Persistence of Trailing Vortices," *Journal of Fluid Mechanics, 471*, 2002.

[14]Dacles-Mariani, J., Chow, J.S., Zilliac, G.G., and Bradshaw, P., "Numerical/Experimental Study of a Wingtip Vortex in a Near Field," *AIAA Journal, 33(9)*, 1995.

[15]Duraisamy, K., Sitaraman, J. and Baeder, J., "High Resolution Wake Capturing Methodology for Improved Rotor Aerodynamic Computations," Proceedings of the 61st Annual Forum of the American Helicopter Society, Dallas, Texas, 2005.

[16]Hodges, D. H., and Dowell, E. H., "Nonlinear Equations of Motion for the Elastic Bending and Torsion of Twisted Nonuniform Rotor Blades", NASA TN D-7818

[17]Ormiston, R. A., Hodges, D. H., and Peters, D. A., "On the Nonlinear Deformation Geometry of Euler-Bernoulli Beams, NASA Technical Paper 1566.

[18]Kvaternik, Raymond G., Kaza, Krishna R. V., Nonlinear Curvature Expressions for Combined Flapwise Bending, Chordwise Bending, Torsion, and Extension of Twisted Rotor Blades, NASA TM X-73, 997, 1976.

[19]Johnson, W., "Rotorcraft Dynamics Models for a Comprehensive Analysis," 54th Annual Forum of the American Helicopter Society, Washington D.C., May 20-22, 1998.

[20]Kufeld, R. M., Johnson, W. "The Effects of Control System Stiffness Models on the Dynamic Stall Behavior of a Helicopter", American Helicopter Society 54nd Annual Forum Proceedings, Washington, D.C., May 20-22.

[21]Yep, H., Bousman, W. G., Johnson, W., "Performance Analysis of a Utility Helicopter with Standard and Advanced Rotors", AHS International Technical Specialists Meeting on Aerodynamics, Acoustics, and Test and Evaluation, San Francisco, January 23-25, 2002.

[22]J. Weissinger, "The Lift Distribution of Swept-Back Wings," National Advisory Committee for Aeronautics, Technical Memorandum No. 1120, 1942.

[23]Bagai, A., Leishman, J.G., "Rotor Free-Wake Modeling using a Pseudo-Implicit Technique - Including Comparisons with Experiment," *Journal of the American Helicopter Society*, Vol. 40, No. 3, July 1995, pp. 29-41.

[24]Smith, M. J., Wong, T., Potsdam, M., Baeder, J., and Phanse, S., "Evaluation of CFD to Determine Two-Dimensional Airfoil Characteristics for Rotorcraft Applications," American Helicopter Society 60th Annual Forum, Baltimore, MD, June 7-10, 2004.

[25]Leishman, J. G., Beddoes, T. S., “A Semi-Empirical Model for Dynamic Stall,” *Journal of the American Helicopter Society*, July 1989, pp. 3-17.

[26]Yeo, H., and Johnson, W., “Assessment of Comprehensive Analysis Calculation of Airloads on Helicopter Rotors,” Presented at the American Helicopter Society 4th Decennial Specialist’s Conference on Aeromechanics, San Francisco, CA, January 21-23, 2004.

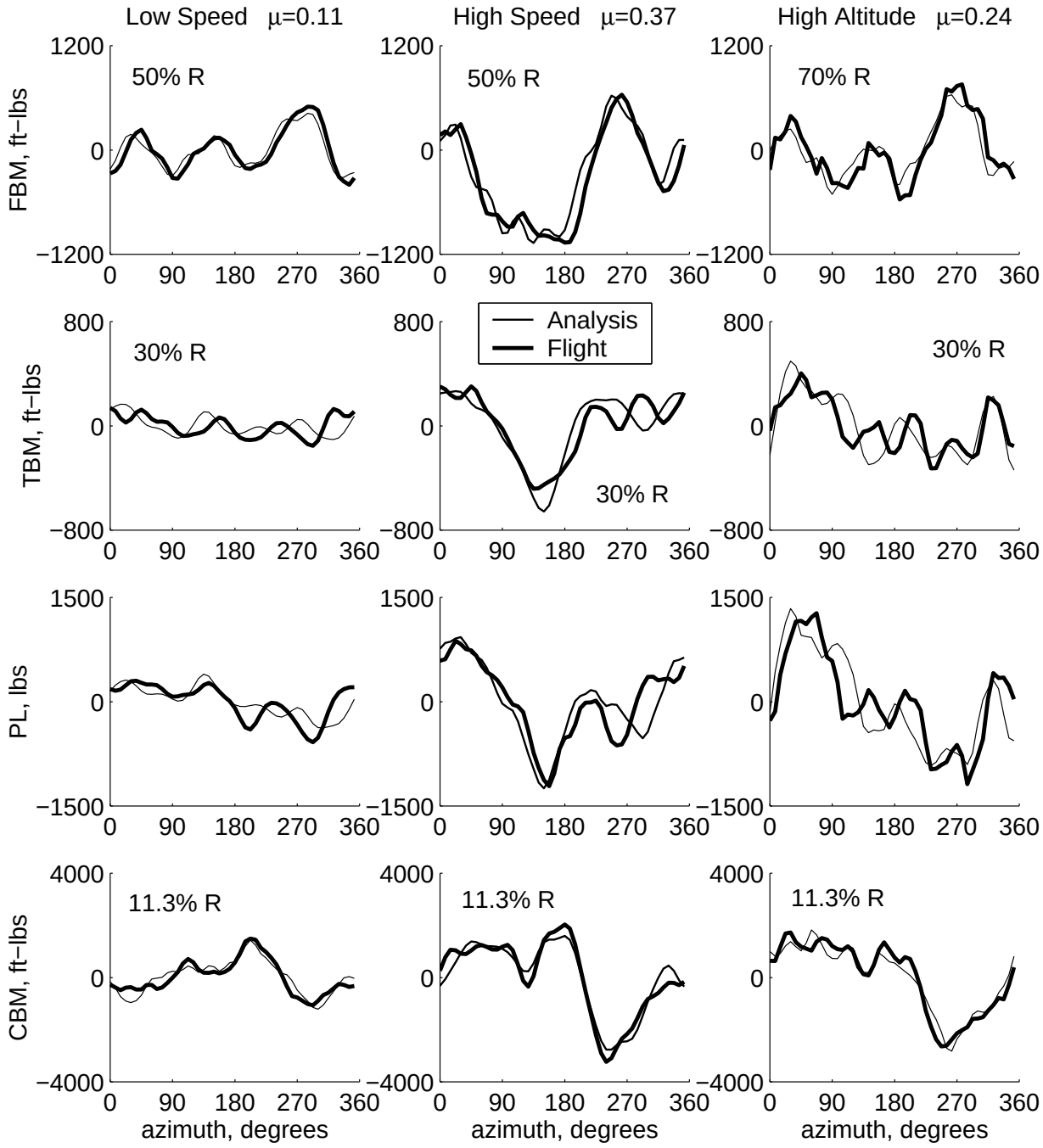

Figure 3: **Validation of CSD model; Predicted structural loads using airloads measured in flight; FBM: Flap Bending Moment, TBM: Torsion Bending Moment, CBM: Chord (Lag) bending Moment, PL: Pitch-Link load; Low speed: flight 8515, High speed: flight 8534, High altitude: flight 9017**

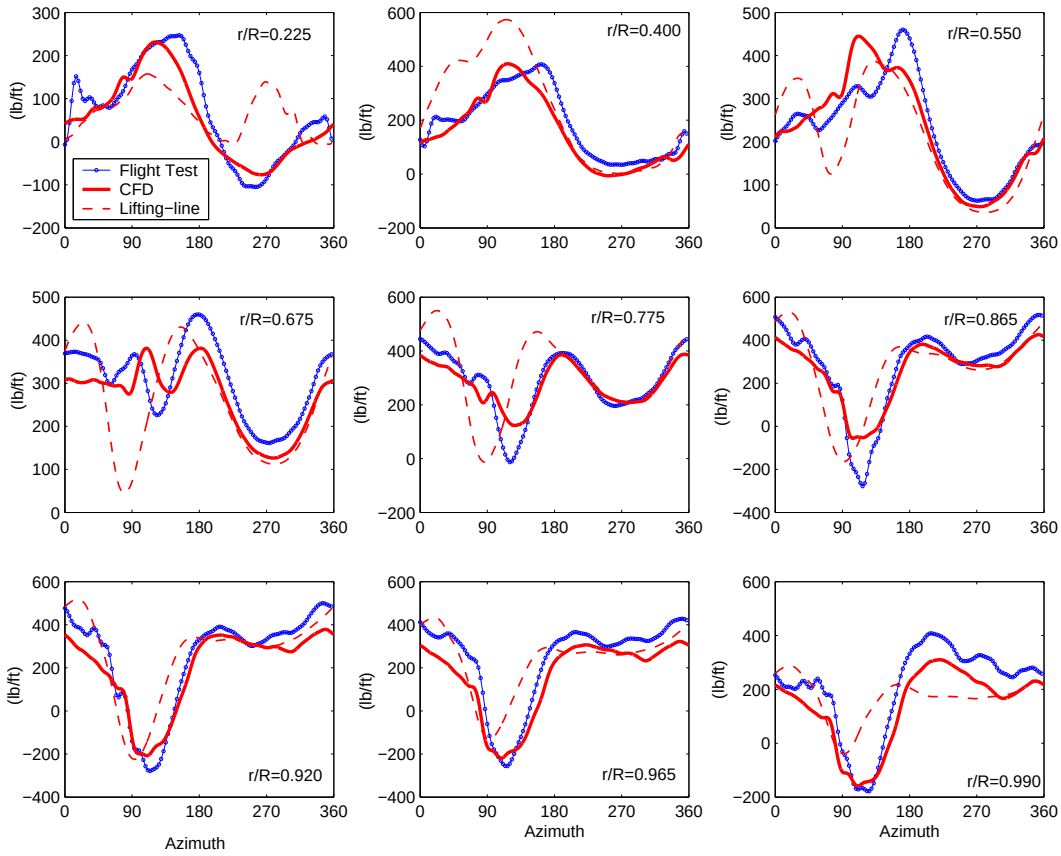

Figure 4: **Sectional Normal Force(0-20/rev) time histories for high speed forward flight 8534**

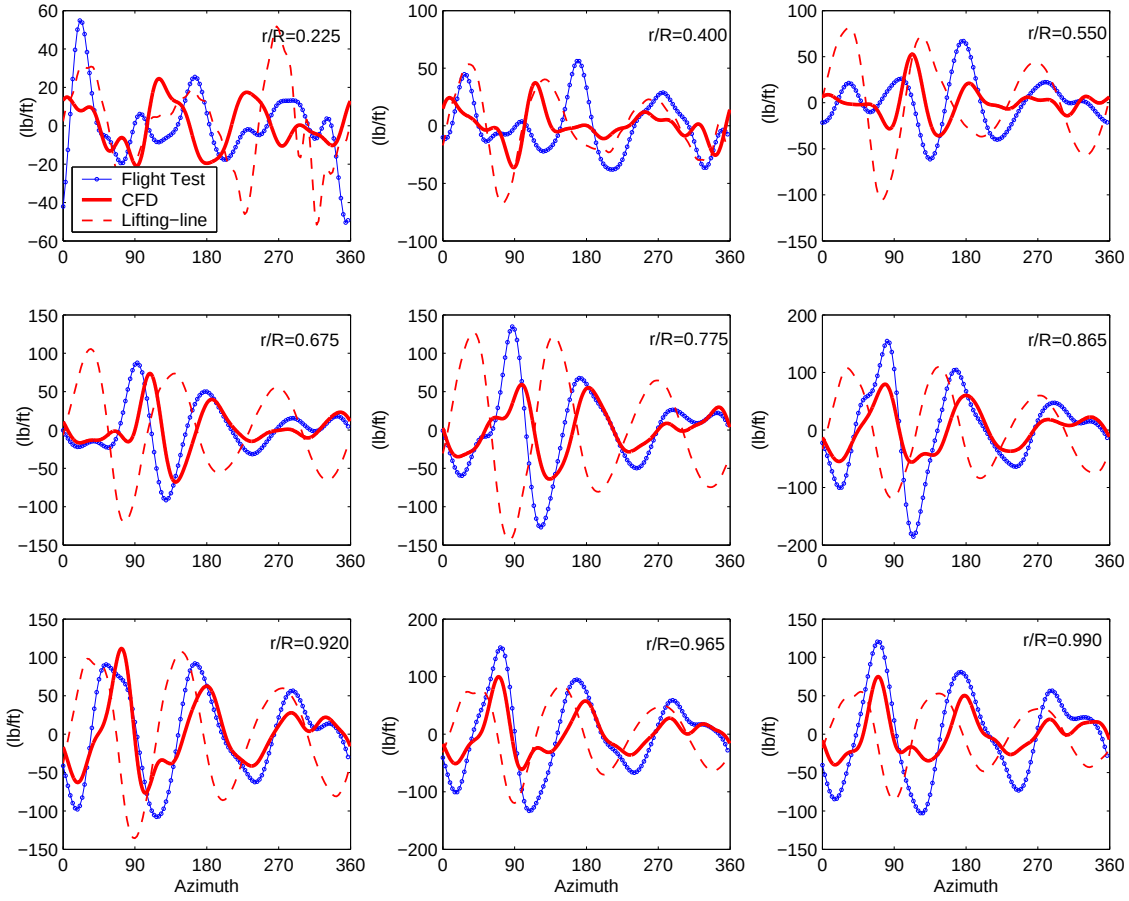

Figure 5: **Sectional vibratory normal Force(3-20/rev) time histories for high speed forward flight 8534**

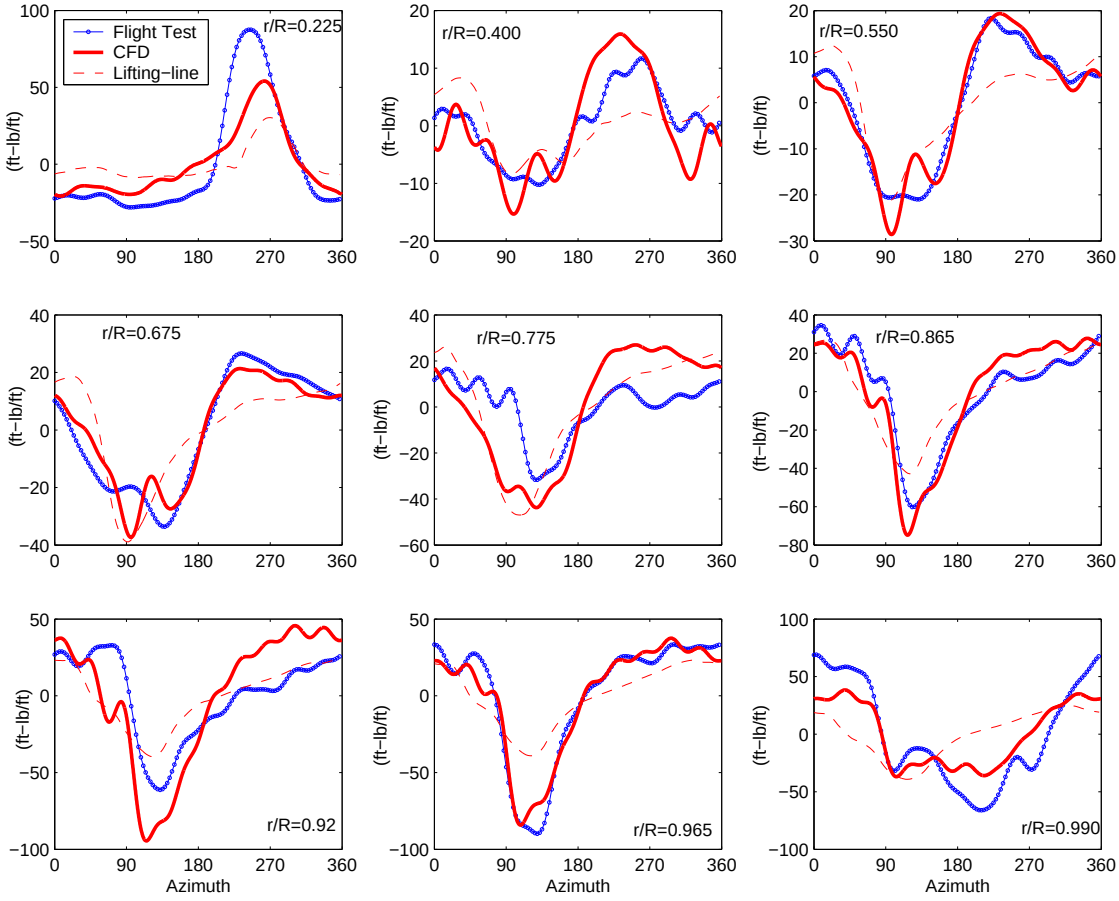

Figure 6: **Sectional pitching moment time histories for high speed forward flight 8534**

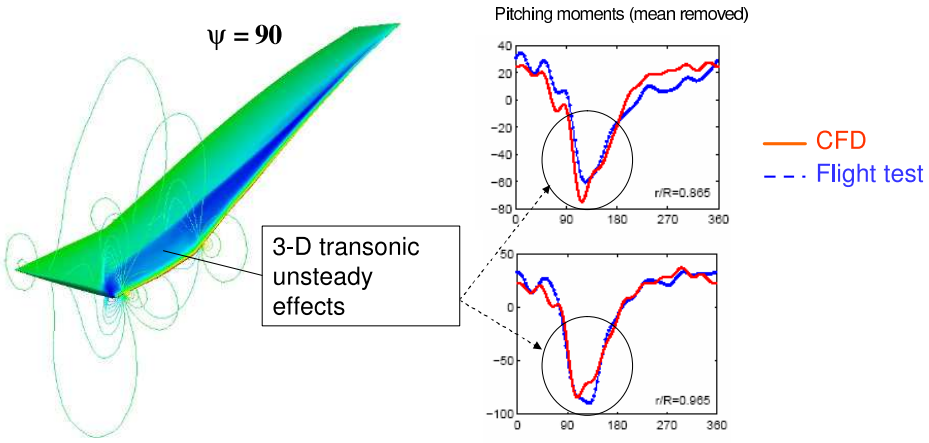

(a) 3-D unsteady transonic effects

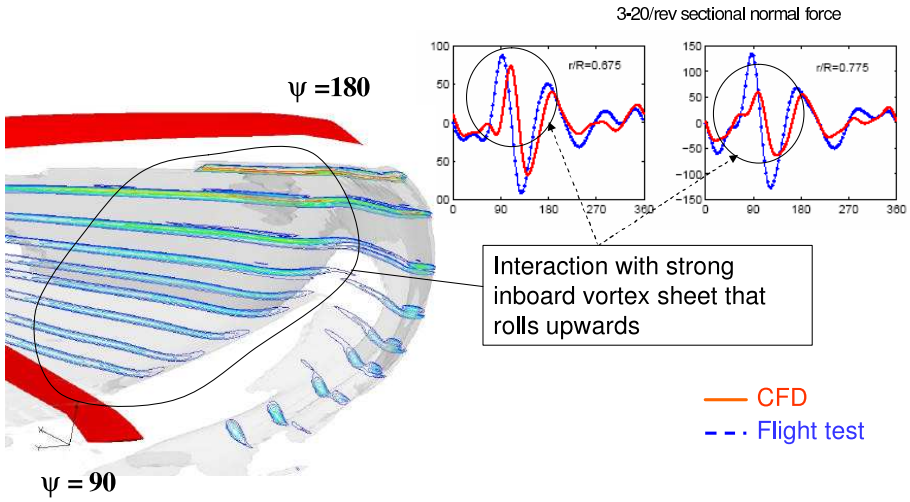

(b) Impulsive loads caused by wake interaction on the advancing side

Figure 7: **Key physical phenomenon that dictate nature of sectional airload time history for the high speed forward flight 8534**

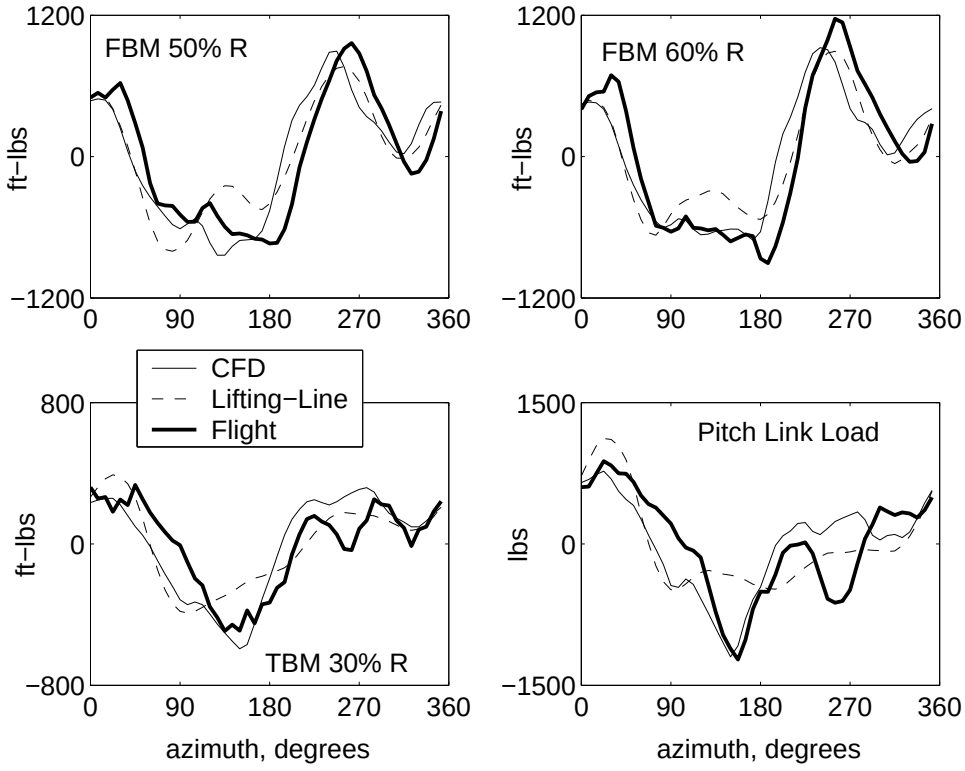

Figure 8: **Predicted structural loads using CFD/CSD coupling for high speed flight 8534**

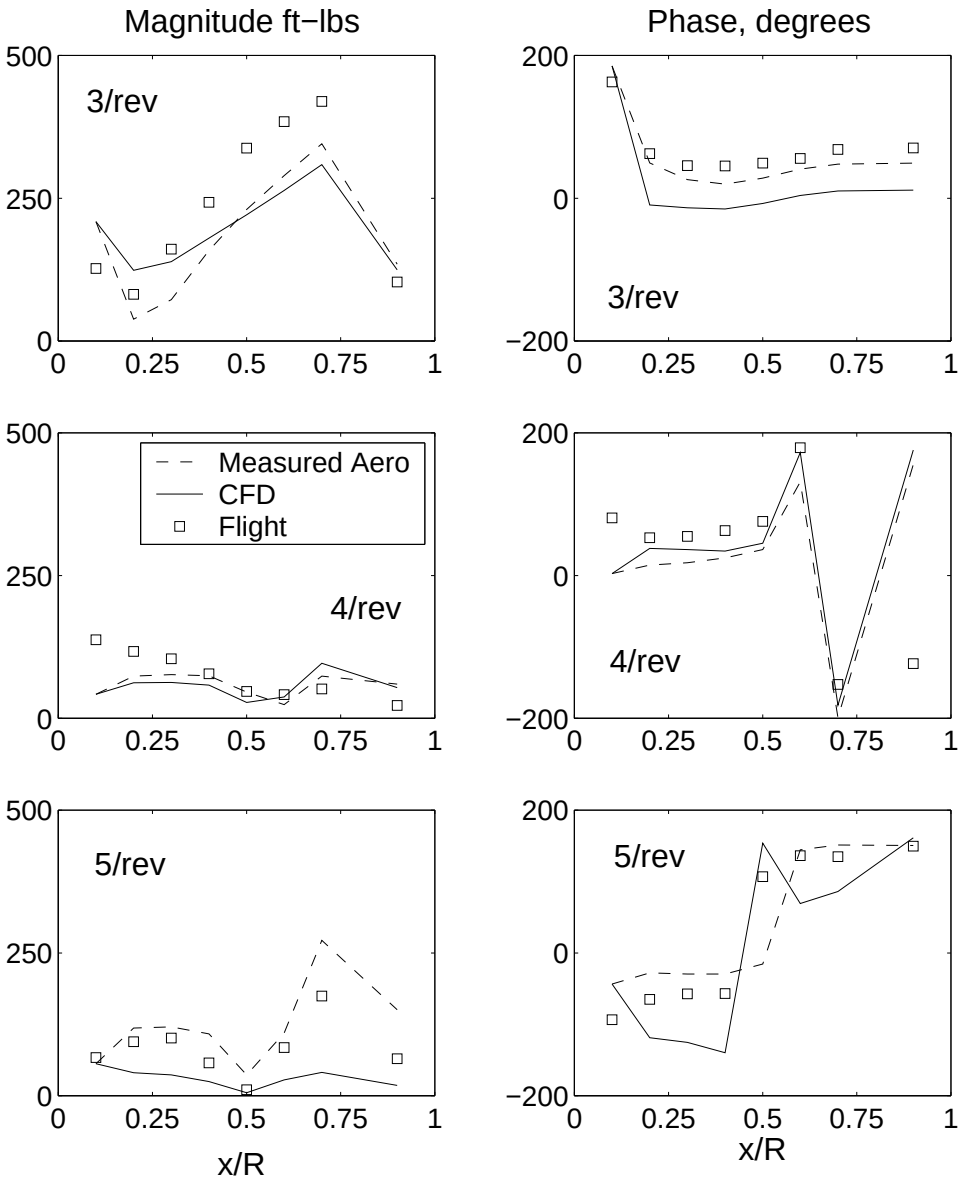

Figure 9: **Predicted vibratory flap bending moments in high speed flight 8534**

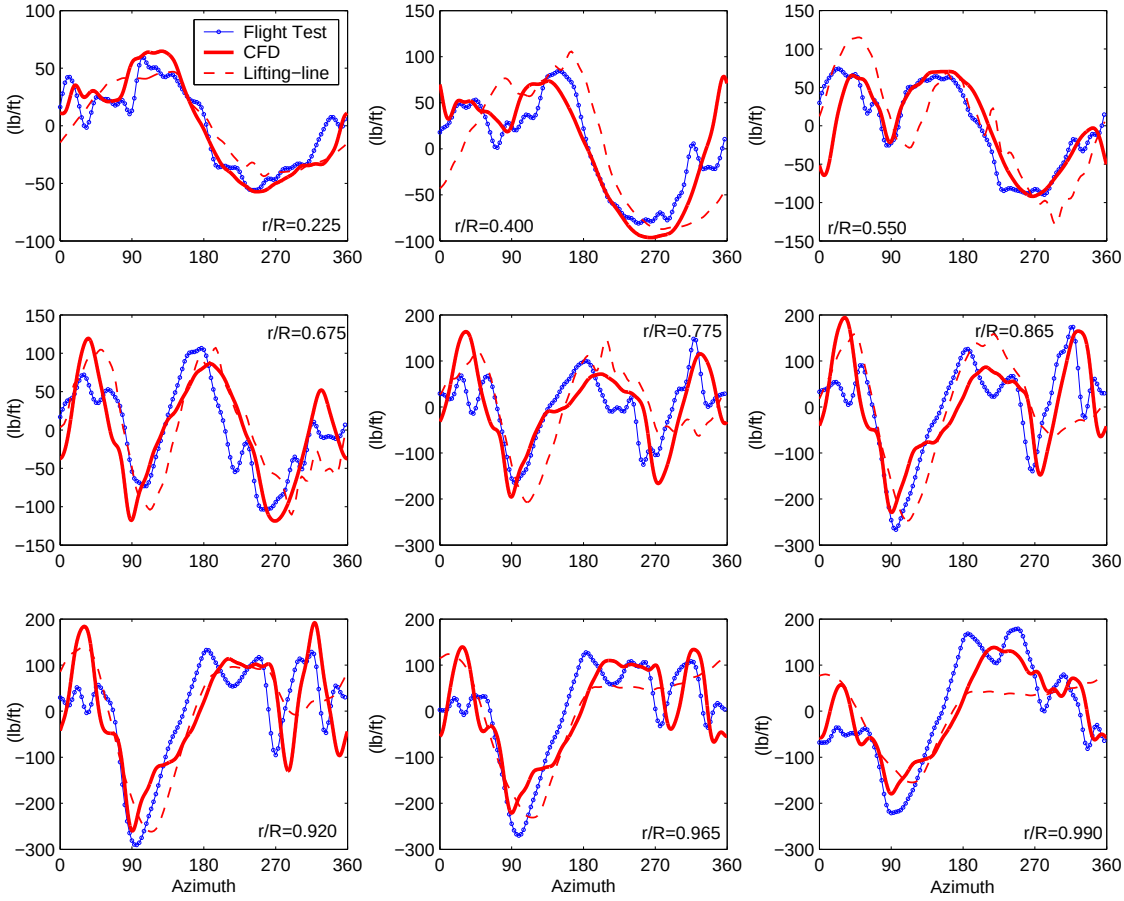

Figure 10: **Sectional normal force (1-20/rev) time histories for high altitude stall flight 9017**

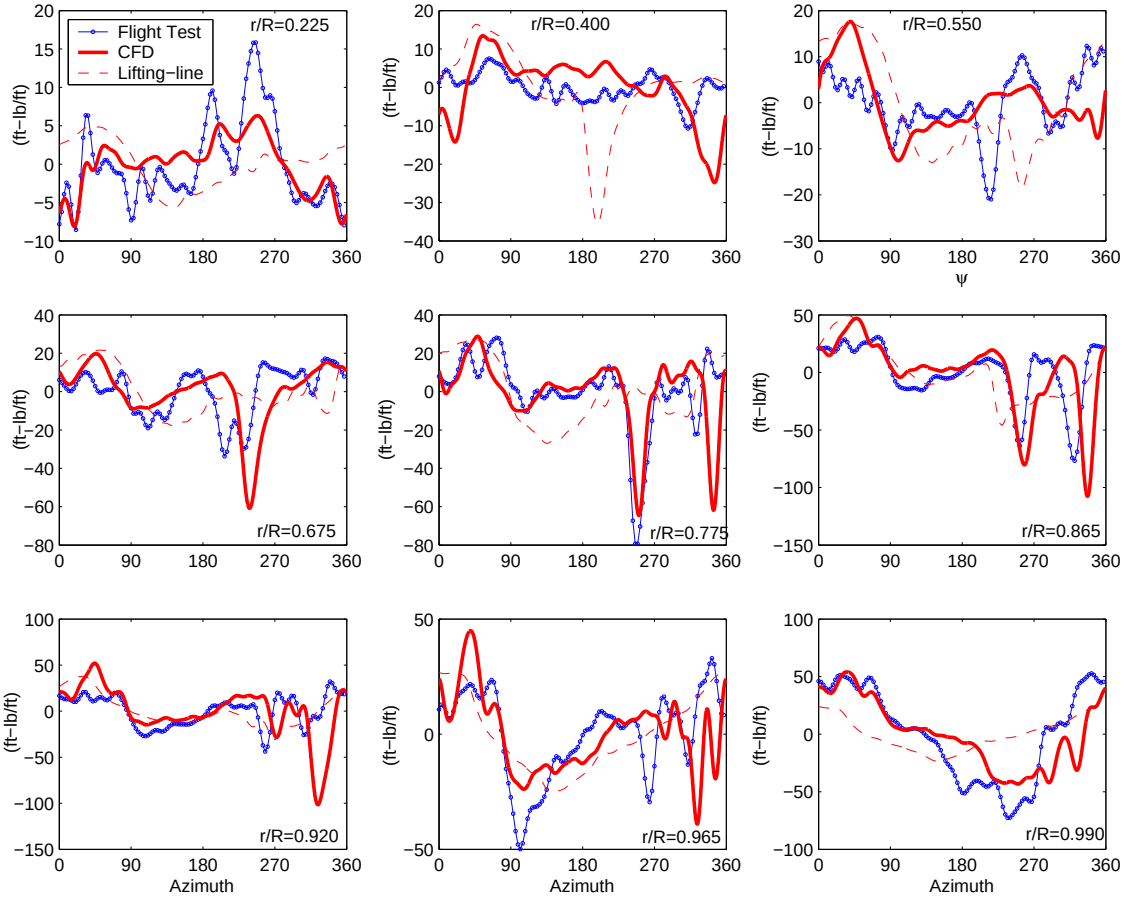

Figure 11: **Sectional pitching moment (1-20/rev) time histories for high altitude stall flight 9017**

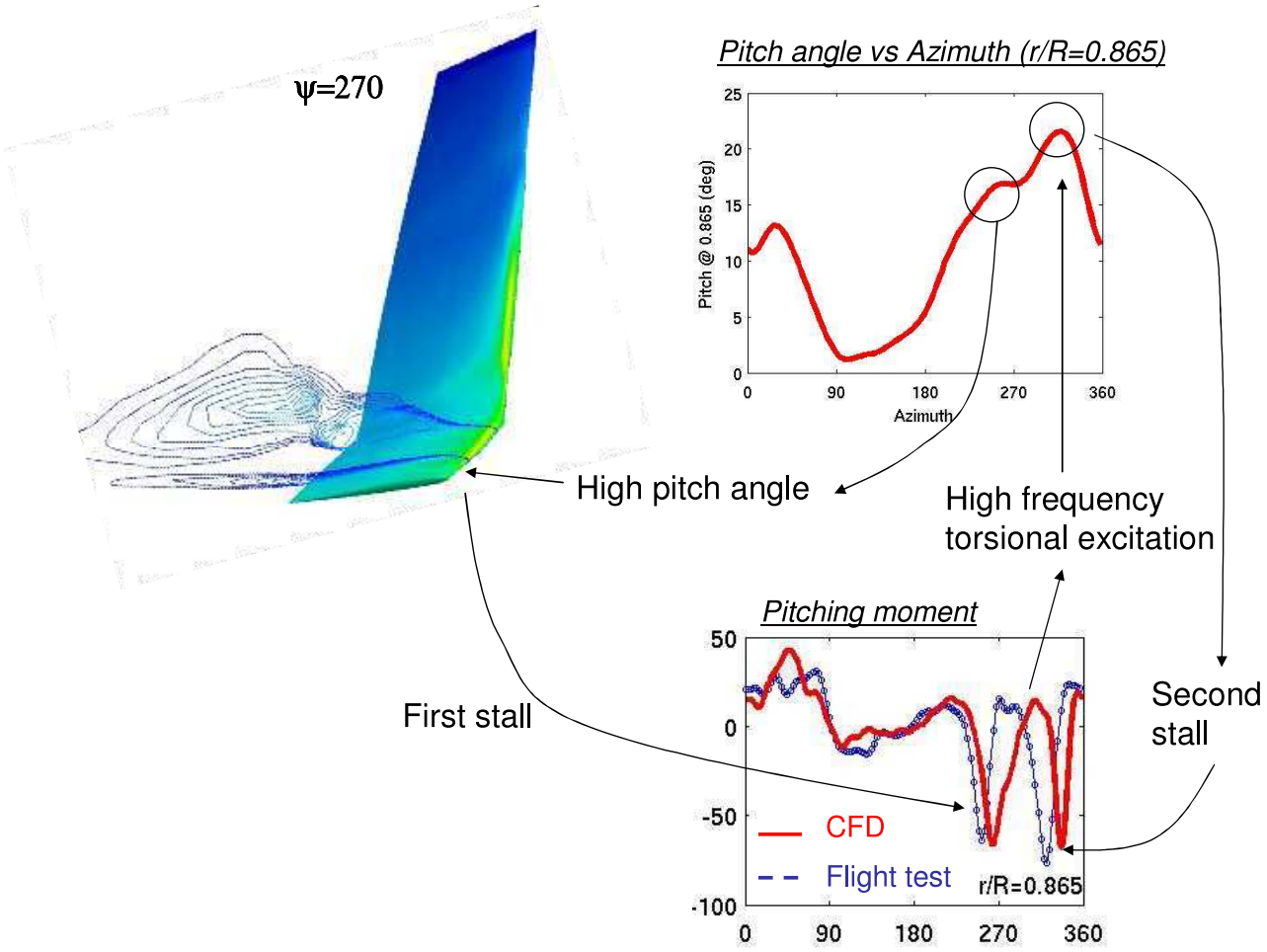

Figure 12: **Key phenomenon that dictate nature of sectional airload time history for the high altitude flight 9017**

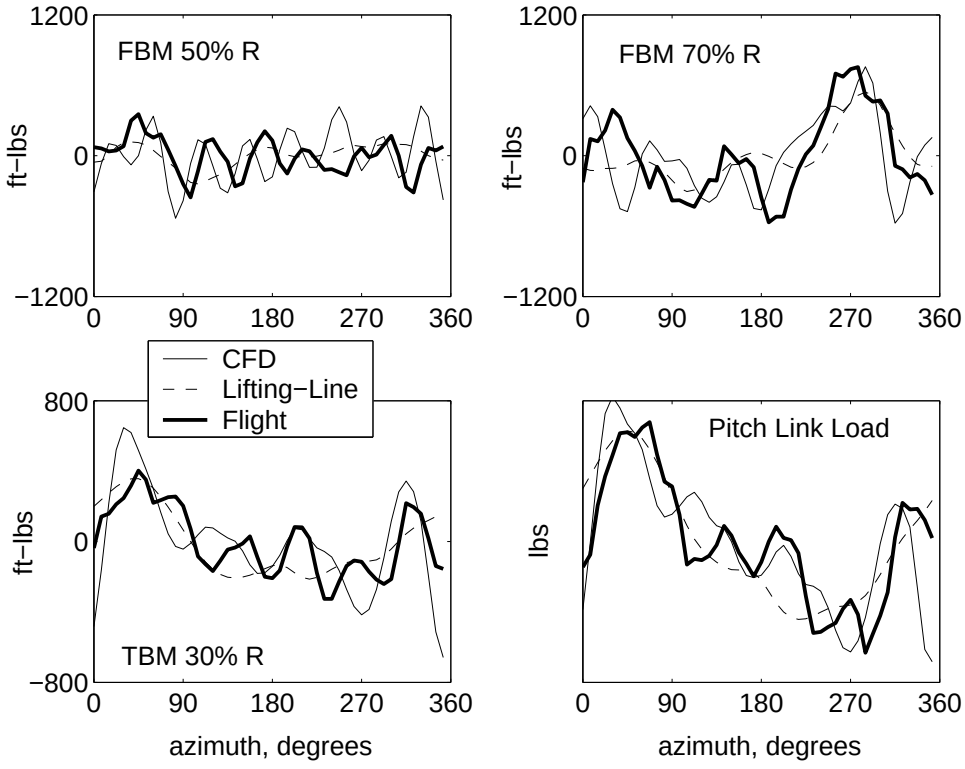

Figure 13: **Predicted structural loads using CFD/CSD coupling for high altitude stalled flight 9017**

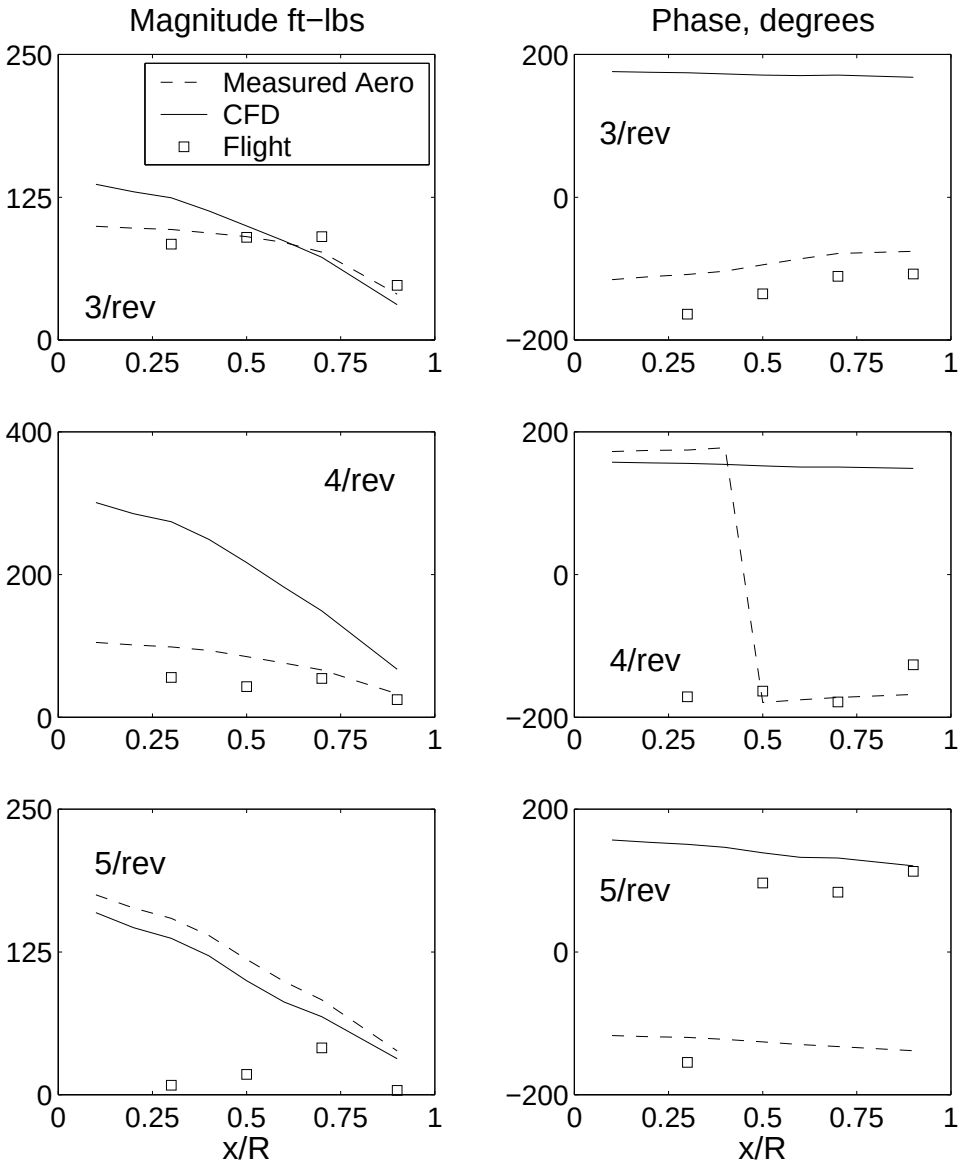

Figure 14: **Predicted 3-5/rev torsion moments in high altitude stall flight 9017**

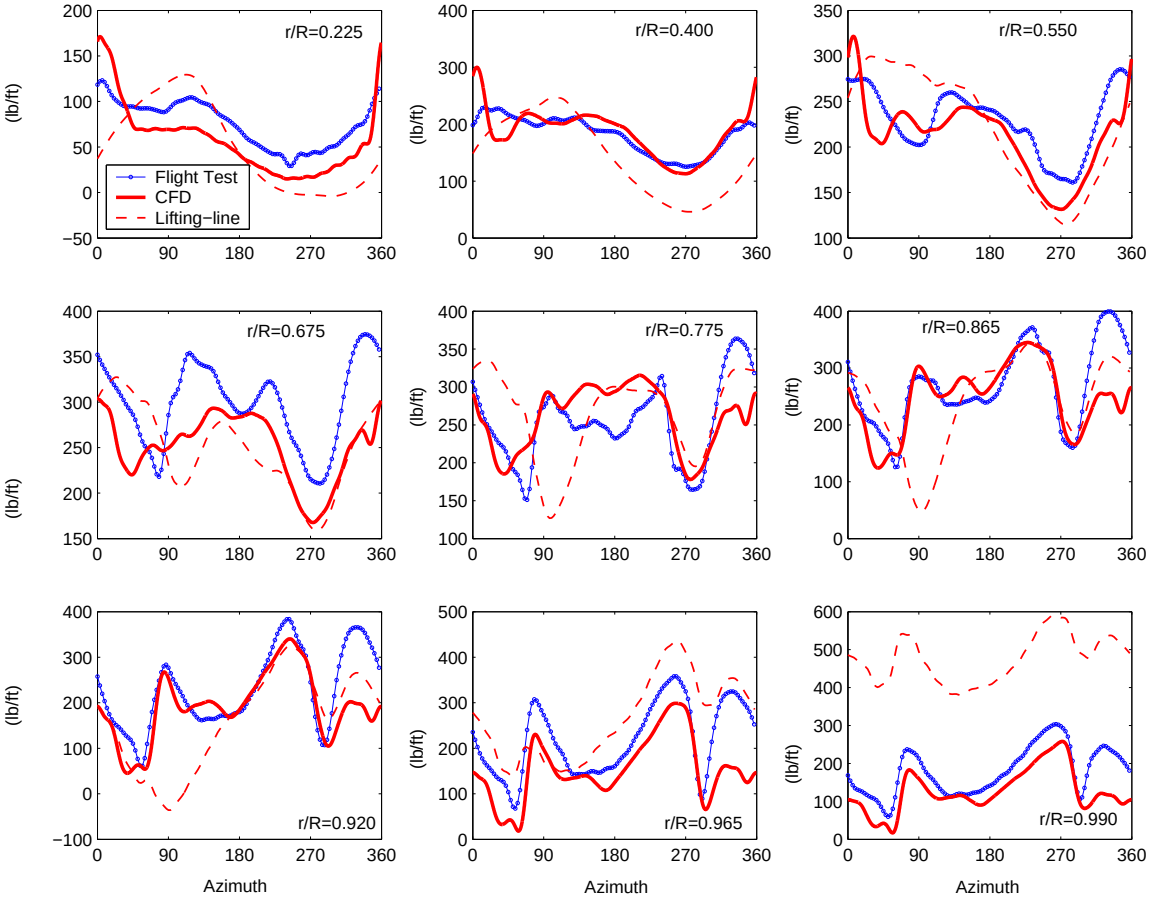

Figure 15: **Sectional Normal Force(1-20/rev) time histories for low speed forward flight flight 8515**

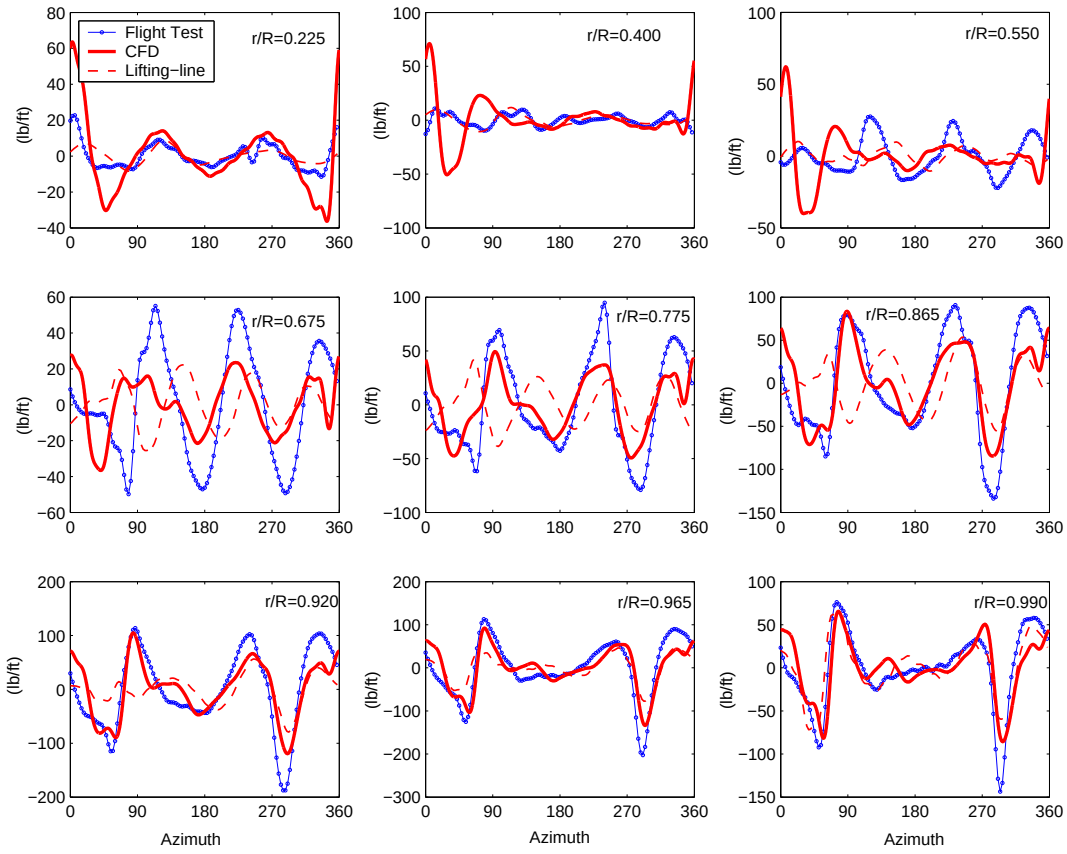

Figure 16: **Sectional vibratory normal Force(3-20/rev) time histories for low speed forward flight 8515**

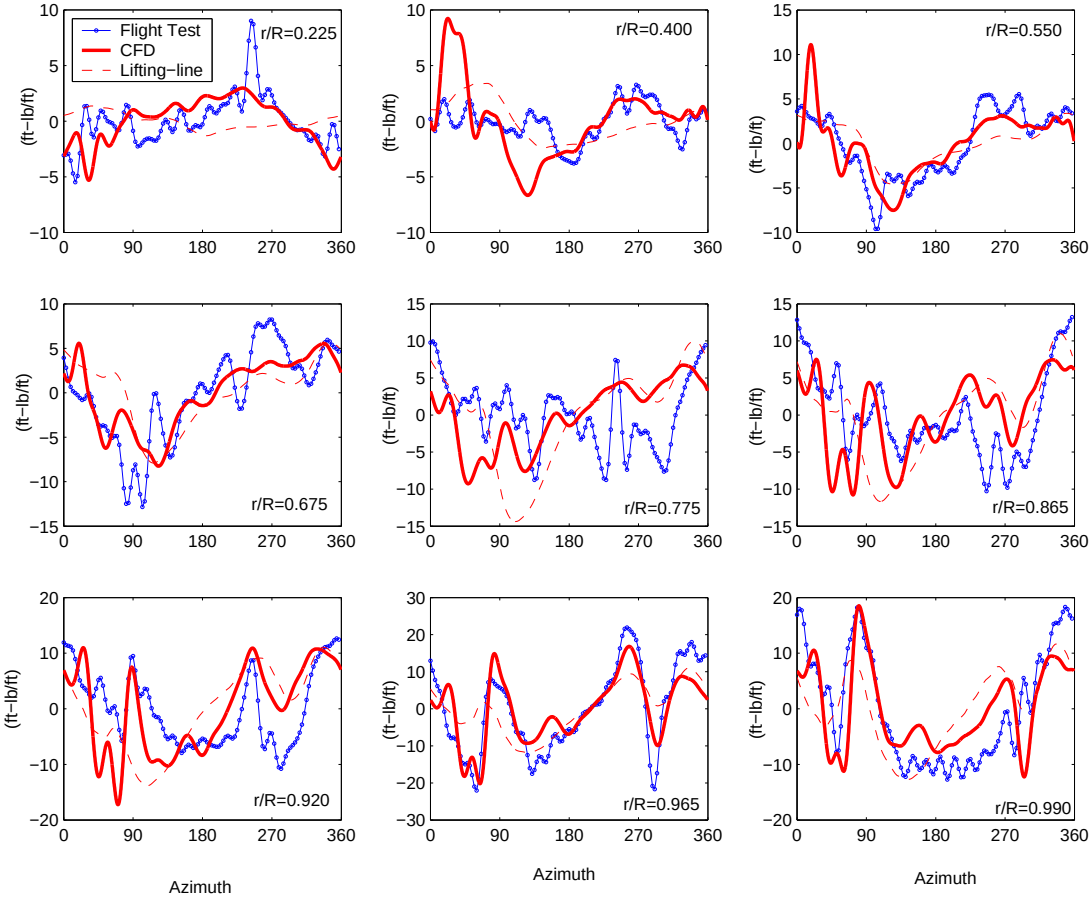

Figure 17: **Sectional pitching moment time histories for low speed forward flight flight 8515**

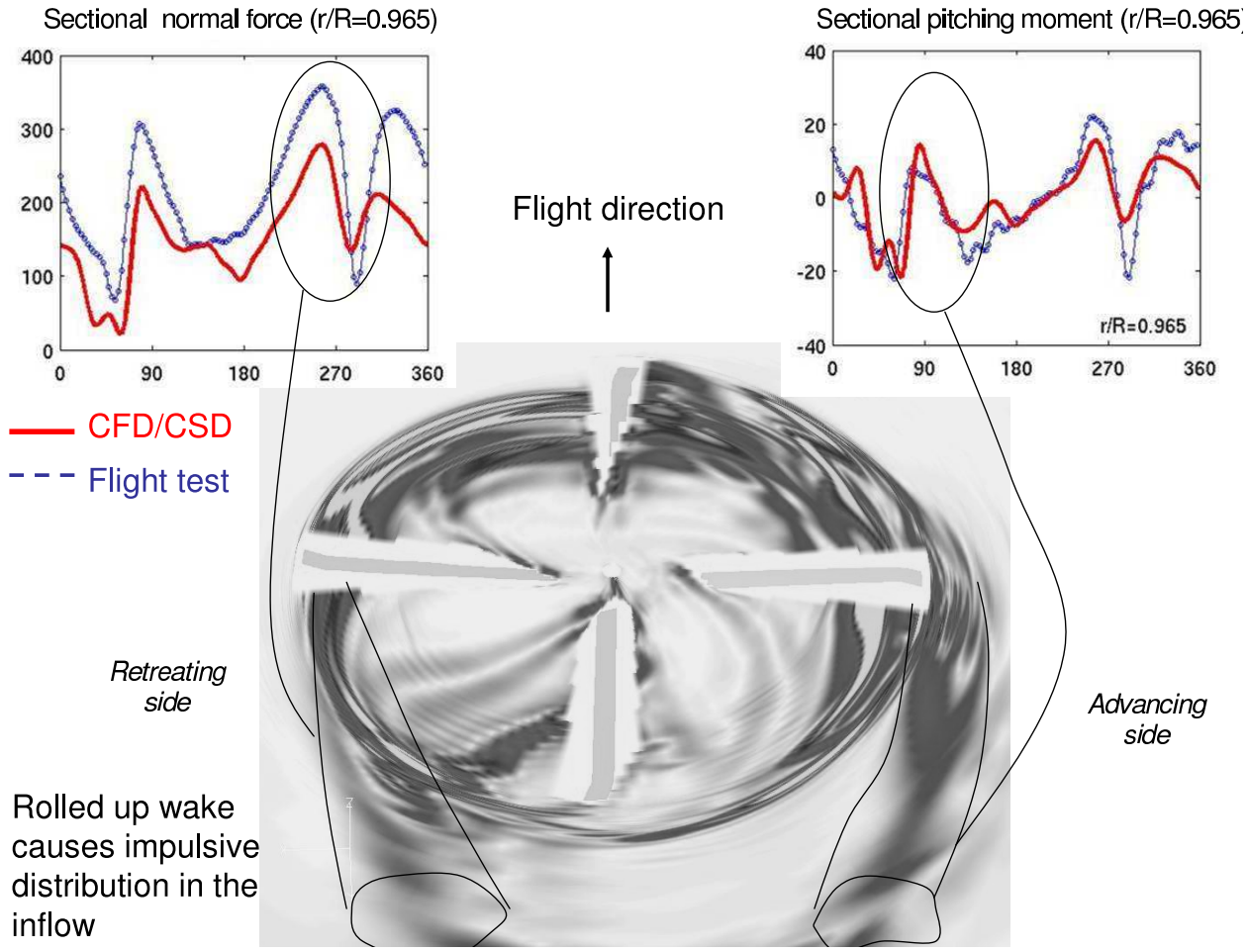

Figure 18: **Key phenomenon that dictate nature of sectional airload time history for the low speed forward flght 8515**

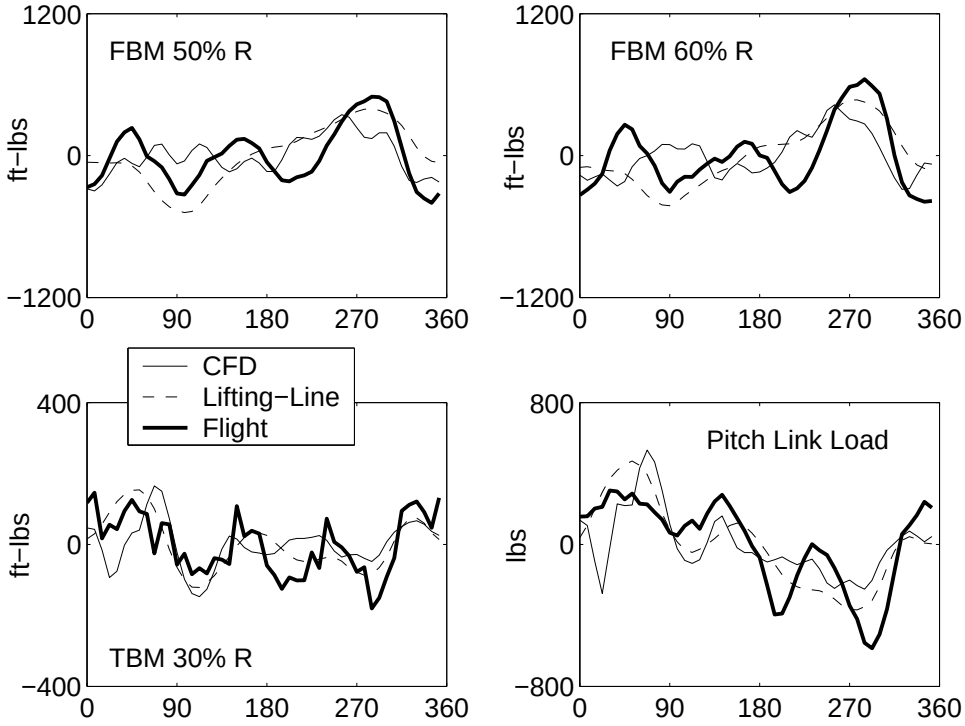

Figure 19: **Predicted structural loads using CFD/CSD coupling for low speed flight 8515**

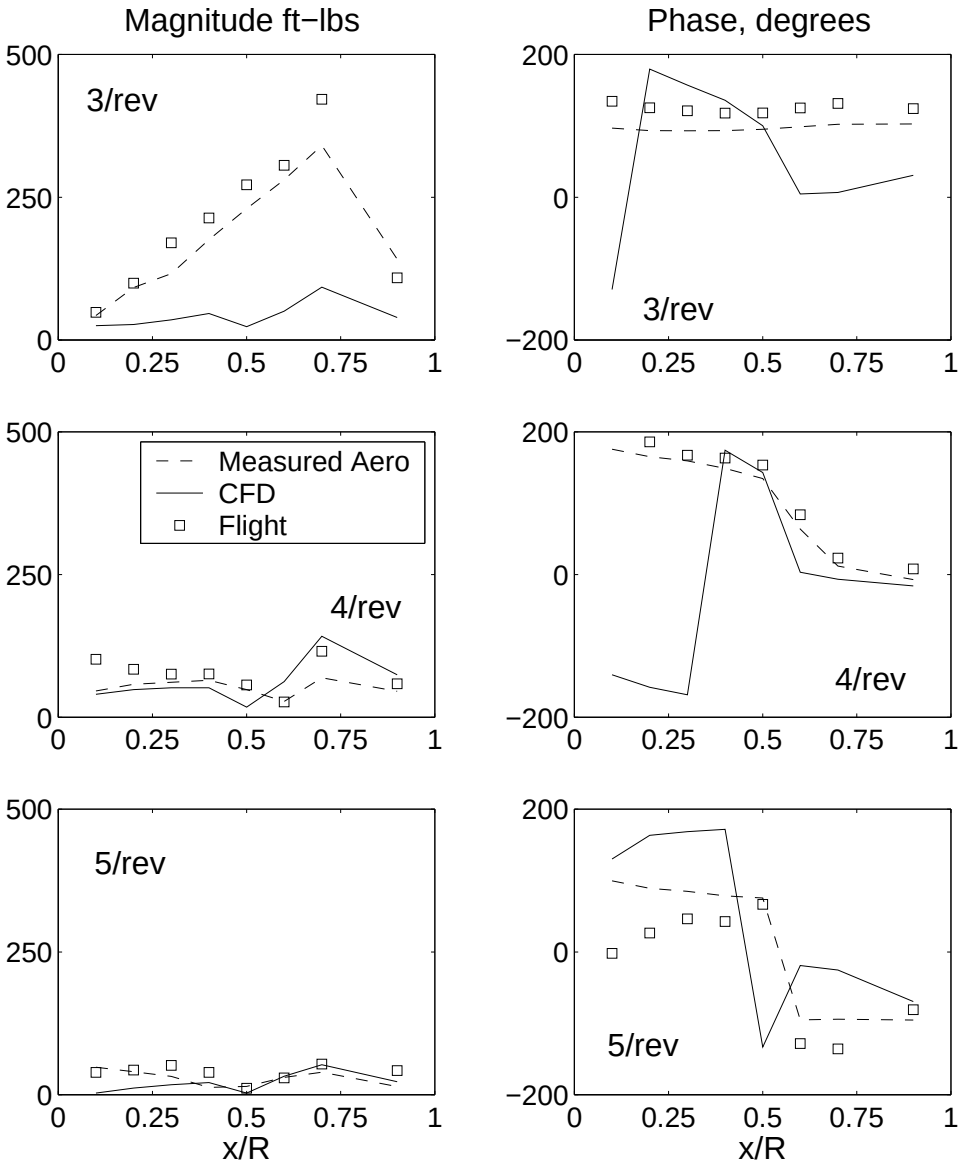

Figure 20: **Predicted vibratory flap bending moments in low speed flight 8515**